Two-photon inner-shell transitions in molybdenum

Yigal B. Bannett and Isaac Freund
Department of Physics, Bar-Ilan University, Ramat-Gan 52100, Israel
(Received 14 October 1983)

The two-photon x-ray emission spectra of inner-shell transitions in metallic Mo have been studied using large-area energy-dispersive Si(Li) detectors and fast, computer-controlled, time-coincidence electronics. The discrete energy-summation spectrum displays a peak at 17.1 keV corresponding to the expected $2s \rightarrow 1s$ transition, as well as a second, more intense peak at 19.7 keV. Based upon very recent analytical H-atom calculations by Florescu, this latter peak is tentatively identified as due primarily to $3d \rightarrow 1s$ transitions. The continuous two-photon spectrum has also been measured on an absolute intensity scale and compared with a frozen-orbital calculation based upon direct summation of the second-order perturbation expansion for the relevant matrix elements. For the $2s \rightarrow 1s$ transition, excellent quantitative agreement is found using the self-consistent-field Hartree-Fock wave functions of Clementi and Roetti. The same calculation predicts that the $3s \rightarrow 1s$ transition is of negligible relative amplitude. Because the calculational method is inapplicable to d states, a simple closure approximation is developed which is found to be reasonably good for both the $2s$ and $3s$ two-photon transitions, but apparently fails for the $3d$ transition since it predicts a result which is relatively much too small. Our data are the first for inner-shell transitions and it is anticipated that further developments in both instrumentation and in theory will yield a new, rich, multiphoton inner-shell spectroscopy.

INTRODUCTION

Although the basic theory of two-photon emission has been available for more than half a century,[1] laboratory experimentation awaited the application of modern beam techniques by Novick and co-workers[2] who pioneered the study of the $2s \rightarrow 1s$ transition in ionized helium. Their basic method was subsequently expanded by Marrus and Schmieder[3] who, in a beautiful series of experiments using the then newly developed beam-foil technology, studied a number of heavy hydrogenic and heliumlike ions. Since that time similar studies have been vigorously pursued by others,[4] resulting in a wealth of additional, fundamental new information.

All these experiments have been limited to the study of two-photon transitions from the metastable $2s$ level for which there is no competing strongly allowed one-photon transition. This is because two-photon emission is typically 4—8 orders of magnitude weaker than strongly allowed one-photon emission. Indeed, the importance of the beam technique[2] is that it yields a nearly pure metastable system downstream of the region in which all strongly allowed one-photon transitions take place. Short-pulse excitation would, in some circumstances, offer a similar advantage.

Of course, two-photon transitions from nonmetastable states are also of intrinsic interest, as is the study of such transitions between the inner shells of many-electron atoms. For such systems beam techniques appear to offer no particular advantage since they cannot be used to eliminate strong one-photon emission. For these systems the only available experimental approach is the straightforward, "brute force" one of detecting the very weak two-photon emission in the presence of an enormously greater one-photon flux. We have been able to accomplish this[5] and consequently have been able to observe, for the first time, two-photon emission from a transition other than $2s \rightarrow 1s$. Our data are also the first for inner-shell transitions. In the following sections we describe in some detail our experimental apparatus and the data obtained and also discuss new theoretical results for many-electron atoms.

PRELIMINARY CONSIDERATIONS

As in all previous work[2-4] we use a pair of identical detectors to collect both emitted photons in fast time coincidence. This serves to minimize the effects of the large one-photon background. The observation of a coincidence event, however, does not guarantee that true two-photon emission has been observed. In addition to fast atomic cascades that appear coincident on the $\sim 10^{-7}$-sec time scale of our apparatus, there are other true two-photon processes, such as double-Compton scattering[6,7] which may be of appreciable intensity. Also, cross talk between the detectors is an intrinsic problem induced by the large one-photon flux. The elucidation and elimination of such interfering phenomena was, in fact, the most time-consuming part of our work. We discuss these various processes in more detail in the Appendix.

We start by estimating the expected two-photon and one-photon signal rates. For this we use well-known hydrogenic results for the $2s \rightarrow 1s$ two-photon transition and the $2p \rightarrow 1s$ one-photon transition, respectively. The number of one-photon events recorded by a detector may be written

$$\dot{N}_1 \simeq \dot{N}_0 \omega_K \left[\frac{\Delta\Omega}{4\pi} \right] , \tag{1}$$

where $\dot{N}_0$ is the rate of K-shell vacancy production, ω_K the fluorescence efficiency, and $\Delta\Omega$ the collected solid angle. In the process of two-photon emission there is only a weak angular correlation between the photon directions, so we may write for the two-photon count rate

$$\dot{N}_2 \simeq \dot{N}_0 \omega_K \left[\frac{\Delta\Omega}{4\pi}\right]^2 \frac{W^{(2)}}{W^{(1)}} . \tag{2}$$

Here the W are the appropriate transition rates. For our hydrogenic model we have[8]

$$W^{(1)} \simeq 6\times 10^8 Z^4 , \tag{3a}$$

$$W^{(2)} \simeq 8Z^6 , \tag{3b}$$

where Z is the nuclear change. Equation (2) suggests that for reasonable count rates $\Delta\Omega/4\pi$ should approach unity. This is not possible with high resolution crystal spectrometers for which this factor is not likely to exceed 10^{-4}. Accordingly, we use large area Si(Li) energy-dispersive detectors which, when closely coupled to the sample, yield $\Delta\Omega/4\pi = 0.10$. For Mo ($Z=42$) we then obtain $\dot{N}_2/\dot{N}_1 \simeq 2\times 10^{-6}$. Although this important ratio could be somewhat improved by going to even heavier elements, this improvement is more than offset by the additional experimental problems involved in the use of very short wavelength x rays.

The actual two-photon count rate may be controlled by adjusting $\dot{N}_0$, so that in principle at least, $\dot{N}_2$ can be made quite large. In practice, the limiting factor here is the maximum one-photon flux the detectors can handle before saturation sets in. In our apparatus this limit is $\dot{N}_1 \lesssim 10^4$/sec, so that $\dot{N}_2 \simeq 1$/min.

The strong one-photon spectrum of Mo consists of the $K\alpha$ and $K\beta$ lines at ~ 17.4 and ~ 19.6 keV, respectively, the L lines at ~ 2.3 keV, and nothing in between. In two-photon emission the ~ 17 keV, $2s \rightarrow 1s$ transition energy, for example, is divided between the two photons, so that for the most part the energy of each falls in the empty spectral window between the L and K lines. Accordingly, with an adequate level of energy discrimination the one-photon flux need not be a problem and, in principle, time coincidence detection should not be necessary. In practice, however, because of incomplete charge collection effects in the detectors, the strong K-line flux tails throughout the region below 17 keV so that an effective background rate $\dot{n}_1 \simeq 2\times 10^2$/sec exists. This enters the coincidence circuitry, whose effective time resolution is $\tau \approx 250$ nsec and produces a false coincidence rate $\dot{n}_1^2 \tau \approx 1$/min. How this background, which is of the same order as the signal, is separated from the signal itself is discussed in the next section.

There are two questions regarding the two-photon spectrum which are of primary interest. (i) What are the relative intensities of different transitions (i.e., $2s \rightarrow 1s$ versus, for instance, $3s \rightarrow 1s$)? (ii) For a given transition, how is the total transition energy divided among the photons? The answer to (i) may be found by summing the energies of the two photons for each event and then plotting the number of events against this energy sum. The resulting spectrum is expected to display discrete peaks corresponding to different transitions and the relative intensities of these should correspond to the relative two-photon transition rates. The answer to (ii) is contained in the differential transition rate $dW^{(2)}/d\omega$. However, theory[1,9] indicates that this may be written

$$\frac{dW^{(2)}}{d\omega} = \frac{2r_0^2 \omega_1 \omega_2}{\pi c^2} |M(\omega_1,\omega_2)|^2 \left[\frac{\Delta\Omega_1}{4\pi}\right]\left[\frac{\Delta\Omega_2}{4\pi}\right] , \tag{4}$$

where the subscripts 1 and 2 refer to the photons and the other symbols retain their usual meanings. Since the interesting spectral information is contained in the matrix element $M(\omega_1,\omega_2)$, we use Eq. (4) to reduce our data and display our experimental results by plotting the absolute value of this matrix element.

EXPERIMENTAL APPARATUS, DATA ANALYSIS, AND RESULTS

Our experimental geometry is shown schematically in Fig. 1. The Mo mask separating the detectors served to minimize the problem of direct, photon-mediated cross talk between them; this is discussed further in the Appendix. The shape of the Si(Li) crystals[10] and the angle between them were chosen, after detailed analysis, to yield maximal coupling to the sample within the constraints imposed by the detector housings. The effective solid angle subtended by each detector was 1.3 sr. The sample chamber, into which the detectors protruded, was evacuated, thereby minimizing (i) air absorption, troublesome at the low-energy end of the spectrum, (ii) airscattering, resulting in reduced background, and (iii) acoustic coupling between the detectors which, because of their large area, acted as sensitive microphones. Further problems due to detector microphonics were minimized by restricting access to the laboratory during data collection and a "talk softly" admonition.

The samples were thin, ~ 100-nm, Mo films sputtered onto 6-μm Mylar foils. This arrangement effectively eliminated self-absorption, permitting low-energy photons to reach the detectors. It also served to minimize cross talk between the detectors mediated by photons scattered

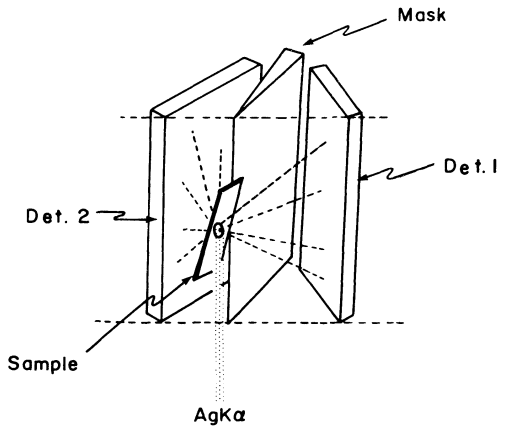

FIG. 1. Experimental geometry. The aspect ratio of the detectors is 3.5:1 and the angle between them is 60°. The angle between lines connecting the sample and detector centers, i.e., the mean angle of emission between the two photons, is very nearly 90°.

through the sample. Finally, the minimal sample mass reduced the intensity of competing effects such as double-Compton scattering to unimportant levels. These matters are discussed further in the Appendix.

K-shell vacancy production was obtained by means of Ag $K\alpha$ radiation from a sealed x-ray tube whose output was filtered through an Ag-Pd-Ag sandwich of 2-mil foils (1 mil$\equiv 10^{-3}$ in.). This filter arrangement was found after extensive testing to yield a maximal signal-to-background ratio. As shown in Fig. 1, the Ag radiation proceeded vertically, intercepting the sample at the detector midplane. The sample plane itself was tilted $\sim 6°$ from the vertical and the sample was surrounded by additional masks which served to further isolate the detectors one from another.

The electronics consisted of the usual pair of dual parallel channels in which the fast channels provide timing information and the slow channels precise energies. Because of the large detector areas (410 mm^2 each) and the concomitant large electronic noise level, the major experimental problem here was achieving good timing with high throughput at the low-energy end of the spectrum. A number of common schemes were tried. The best proved to be simple leading-edge timing preceded by a moderate degree of pulse shaping. Since the energies were accurately known from the slow channels, the energy-dependent walk intrinsic to this timing scheme could be subsequently corrected for during data analysis.

In order to prevent severe pulse pileup in the slow channels due to the high initial count rate and the very long ultimate pulse integration times, the slow amplifier chains were split at a point preceding the final long-time-constant shaping. The signals were routed through delay amplifiers and then through low-noise analog gates controlled by the time-coincidence circuitry, after which they were returned to the final shaping stages of the amplifiers. In this way only pulses corresponding to near-coincidence events in the right energy interval engaged the final shaping circuitry. Because of constraints imposed by electronic noise at the low-energy end and tailing of the Mo $K\alpha$ line at the high-energy end, the spectral region accepted in this work was ~ 4—14 keV.

The outputs of the analog electronics were digitized by fast 8-bit (binary digit) analog-to-digital converters (ADC's) and transferred under interrupt control to an on-line Apple II+ microcomputer. During a typical month-long data run in which the detectors collected $\sim 5\times 10^{10}$ events, a total of $\sim 30\,000$ events satisfying both the time and energy criteria were recorded. Of these, $\sim \frac{2}{3}$ were true two-photon events. Each event recorded was characterized by four numbers: the difference in arrival time of the two photons Δt measured in the usual way with the aid of a time-to-amplitude converter (TAC), their respective energies, E_1 and E_2, and the clock time at which the event occurred. A data table containing this information was subsequently transferred to a large mainframe computer for off-line processing.

Data analysis proceeded as follows. The data table was first scanned for spurious bursts of coincidences identified via the clock-time entry. These were presumably caused by power-line fluctuations (a particularly severe local problem), RF interference, and other causes. These bursts, which accounted for $\sim 0.5\%$ of the data were eliminated from further consideration. The remaining entries were then placed on an absolute energy scale using calibration data recorded under conditions which closely mimicked those obtaining during the actual run. This latter precaution proved necessary because of count-rate

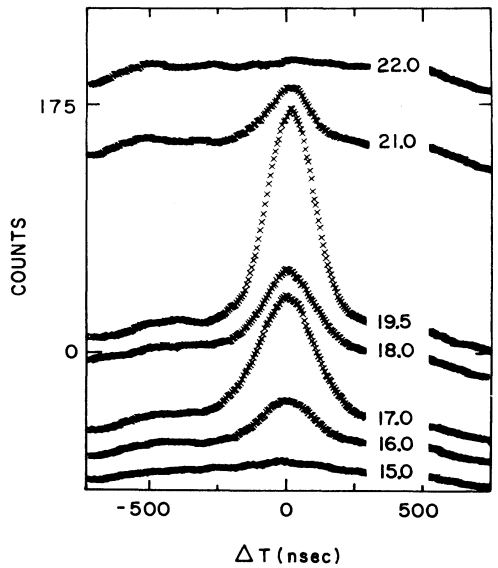

FIG. 2. TAC spectra for events in which the energy sum E_1+E_2 falls within a 1-keV window centered at different values between 15.0 and 22.0 keV. The rounding at the edges of the spectra is due to data collection within a bounded time interval and the subsequent walk correction.

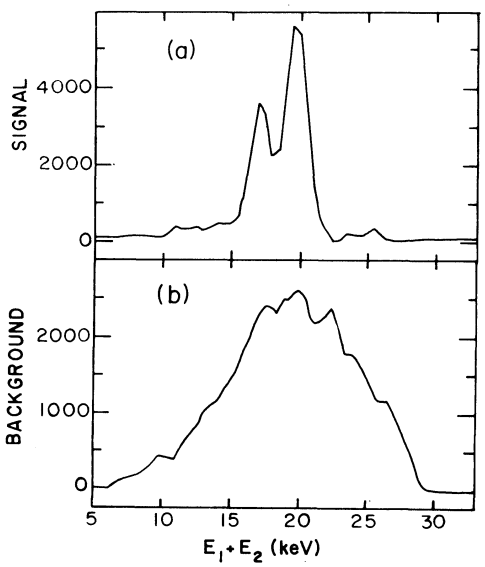

FIG. 3. (a) Two-photon intensity vs energy sum E_1+E_2. The two peaks are centered at 17.1 and 19.7 keV, respectively. (b) Spectrum of random coincidences vs energy sum E_1+E_2. The shape of this spectrum, which in principal should be flat, is determined by the rounding due to data collection within a bounded energy interval 4—14 keV and by various energy-dependent losses.

dependent amplitude shifts in the analog circuitry. The Δt's were next corrected for walk using the known pulse energies and appropriate calibration data also obtained under run-time conditions. From this corrected master table appropriate subtables were constructed as required.

True two-photon events are characterized by an energy sum 17 keV $< E_1 + E_2 < 20$ keV and $\Delta t = 0$. For the random one-photon coincidences, on the other hand, E_1 and E_2 are uncorrelated and all values of Δt are equally probable. Accordingly, from our master table we constructed subtables of all events for which the energy sum fell within a 1-keV window centered at some predetermined value and for each such table we plotted a histogram as a function of Δt. When $E_1 + E_2$ falls outside the region 17—20 keV the resulting historgrams should be flat, while when $E_1 + E_2$ falls within this region a peak centered at the origin should appear. The data, shown in Fig. 2, are in complete accord with this expectation. After extrapolating the nearly flat background under the peaks in Fig. 2, we plotted the net peak areas as a function of the energy sum with the results shown in Fig. 3(a).

Since the individual detector response functions are very well represented by Gaussians of variance Δ_1 and Δ_2, respectively, each of the peaks in Fig. 3(a) should be described by

$$F(E_1+E_2, E_T, \Delta E) = \mathrm{erf}(\epsilon_+) - \mathrm{erf}(\epsilon_-) , \tag{5}$$

where E_T is the transition energy (peak center), $\epsilon_\pm = (E_1 + E_2 - E_T \pm \Delta E/2)/(\sqrt{2}\Delta)$, $\Delta^2 = \Delta_1^2 + \Delta_2^2$, and $\Delta E = 1$ keV. For our system $\Delta = 0.67$ keV, so that the full width at half maximum of Eq. (5) is 1.7 keV. The observed data are extremely well represented by two peaks each of the form of Eq. (5) with transition energies of 17.1 and 19.7 keV, respectively. The former corresponds to the $2s \rightarrow 1s$ transition of Mo, while the latter is tentatively identified as due to $3d \rightarrow 1s$.

In view of the complexity of the analog circuitry and in order to verify that the apparatus really behaved as we thought it did, we constructed a computer model which incorporated the measured response functions of each of the electronic modules and the various interactions between these. We then processed a variety of simulated spectra through this model and compared the results with the measured data. The agreement was excellent and confirmed the correctness of such features as the rounding seen in Fig. 2 for the random-coincidence background and the shape of the random-coincidence energy-summation spectrum shown in Fig. 3(b). Accordingly, we conclude that our apparatus was well-behaved and that the data obtained are reliable.

In order to obtain experimental values for $|M(\omega_1,\omega_2)|$ [Eq. (4)], for the 17.1-keV transition, for example, we proceeded as follows. We first extracted from our master table all entries for which $E_1 + E_2$ fell within a 1-keV window centered at 17.1 keV and for which $|\Delta t| \leq 250$ nsec. For these events we constructed two historgrams, one as a function of E_1 and the other as a function of E_2. In addition to the desired two-photon spectra, these histograms also contained the spectrum of the random one-photon coincidences. Accordingly, after suitable normalization, we subtracted this off. (The requisite random-coincidence spectra were obtained as described above except that for these we selected events in which $|\Delta t| > 250$ nsec.) The two-photon spectra were next corrected for absorption losses in the apparatus, the energy-dependent throughput of the analog circuitry, and the fact that in accordance with Eq. (5) and Fig. 3(a) a 1-keV window accepts only part of the events corresponding to a given transition. At this point, if the correction procedures were perfect, the E_1 and E_2 spectra should have been both symmetric and identical. In practice, of course, neither condition was strictly met. We therefore averaged these two spectra in the expectation that this would tend to average out the residual uncertainties in our correction procedures. The 19.7-keV transition was handled in a similar fashion.

The spectra were placed on an absolute intensity scale in the following manner. We converted our measured two-photon count-rate per channel, $d\dot{N}_2/dn$ to a spectral density $d\dot{N}_2/d\omega$ via

$$\frac{d\dot{N}_2}{d\omega} = \frac{d\dot{N}_2/dn}{\hbar^{-1} dE/dn} , \tag{6a}$$

where dE/dn is the energy increment per channel. This measured density is related to $dW^{(2)}/d\omega$, Eq. (4), by

$$\frac{d\dot{N}_2}{d\omega} = \frac{dW^{(2)}}{d\omega} N_{00} , \tag{6b}$$

where N_{00} is the steady-state number of atoms containing K-shell vacancies. This was obtained from the measured flux of Mo $K\alpha$ and $K\beta$ photons $\dot{N}_1$ using

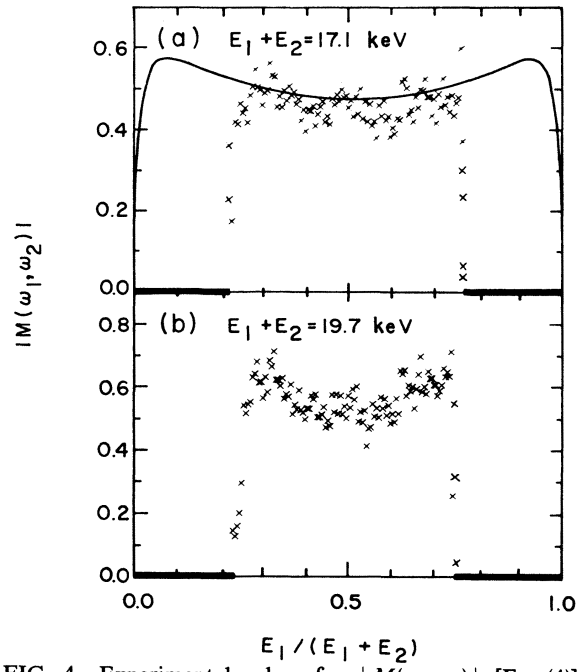

FIG. 4. Experimental values for $|M(\omega_1,\omega_2)|$ [Eq. (4)] vs $E_1/(E_1+E_2)$ for events comprising (a) the 17.1-keV and (b) the 19.7-keV peaks of Fig. 3(a). The data are restricted to a 4—14-keV interval by upper- and lower-level discriminators. The solid line in (a) is the calculated value for the $2s \rightarrow 1s$ transition, Fig. 5(d).

$$\dot{N}_1 = W^{(1)} N_{00} \left[\frac{\Delta\Omega}{4\pi} \right] . \tag{6c}$$

Equations (6) together with Eq. (4) yield $|M(\omega_1,\omega_2)|^2$ in terms of measured quantities and $W^{(1)}$. This latter quantity was calculated from

$$W^{(1)} = \frac{4\alpha}{c^2} (\Omega^3_{2p,1s} |\langle 2p | z | 1s \rangle|^2 + \Omega^3_{3p,1s} |\langle 3p | z | 1s \rangle|^2) \tag{7}$$

using the observed transition frequencies, Ω, and the self-consistent-field Hartree-Fock (SCFHF) wave functions of Clementi and Roetti.[11] Our final results for $|M(\omega_1,\omega_2)|$ are shown as the data points in Fig. 4.

COMPARISON WITH THEORY

As implied by our notation till now (i.e., $2s \rightarrow 1s$, etc.), we make the approximation that the many-electron atomic system may be adequately described by "frozen" orbitals whose form and energy are independent of their degree of occupation. This approximation, which is normally tested first in any new problem, generally correctly reproduces the major features of atomic processes and permits us to describe the two-photon emission in the familiar terms of an electron in an initial state $|I\rangle$ making a transition to a final state $|F\rangle$.

The matrix element $M(\omega_1,\omega_2)$ may be written

$$M(\omega_1,\omega_2) = M(A^2) + M(\vec{p}\cdot\vec{A}) , \tag{8a}$$

where $\vec{A}$ is the vector potential,

$$M(A^2) = (\hat{u}_1\cdot\hat{u}_2)\langle I | e^{i(\vec{k}_1+\vec{k}_2)\cdot\vec{r}} | F\rangle , \tag{8b}$$

and

$$M(\vec{p}\cdot\vec{A}) = (\hbar/m)(1+P_{1,2}) \times \sum_n \langle I | \hat{u}_1\cdot\vec{\nabla} | n\rangle\langle n | \hat{u}_2\cdot\vec{\nabla} | F\rangle / (\Omega_{n,F} - \omega_2). \tag{8c}$$

Here the u's and k's are the photon polarization and wave vectors, respectively, and $P_{1,2}$ permutes the subscripts 1 and 2. Since for a hydrogenic model the product of the photon wave vector and atomic orbital radius is $ka \sim (\frac{3}{8})\alpha Z \simeq 0.15$ for Mo, we have suppressed factors of $e^{i\vec{k}\cdot\vec{r}}$ in Eq. (8c). Note that in this approximation the selection rules for $M(\vec{p}\cdot\vec{A})$ are $\Delta l = 0, \pm 2$, while to lowest nonzero order in $\vec{k}\cdot\vec{r}$ the selection rules for $M(A^2)$ are $\Delta l = \pm 1$. In our present experiment we are unable to distinguish between transitions from sublevels of a given principal shell (e.g., $2p \rightarrow 1s$ vs $2s \rightarrow 1s$), so that the contributions of Eqs. (8b) and (8c) to our measured intensities need be added in quadrature. Since $|M(A^2)|^2 \ll |M(\vec{p}\cdot\vec{A})|^2$ for all transitions from the same shell, we neglect the former and turn to an evaluation of the latter.

We proceed to sum the full series in Eq. (8c). In this we go beyond earlier treatments by Freund[12] and by Aberg,[13] each of whom treated a different subset of terms. The intermediate states involved in Eq. (8c) may be divided into three classes. (i) Empty bound (Rydberg) states. For these the $2s \rightarrow 1s$ transition proceeds via channels such as $(2s \rightarrow 5p \rightarrow 1s)$, etc. (ii) Continuum states. Here the appropriate channels are $(2s \rightarrow p\text{-wave} \rightarrow 1s)$. Note that (i) and (ii) are both double-hole states in the sense that in addition to the initial K-shell vacancy, the intermediate state contains another hole in the original electron manifold. (iii) Single-hole states. Here a typical channel is $(3p \rightarrow 1s)(2s \rightarrow 3p)$. Note that there are only a finite, small number of these. We denote the partial sums corresponding to these three classes by $M^{(\mathrm{Ryd})}$, $M^{(\mathrm{cont})}$, and $M^{(\text{1-hole})}$, respectively. After transforming the matrix elements of the gradient operator into those of the dipole moment operator, we proceed as follows.

$M^{(\text{1-hole})}$: We evaluate the requisite matrix elements directly using the SCFHF wave functions of Clementi and

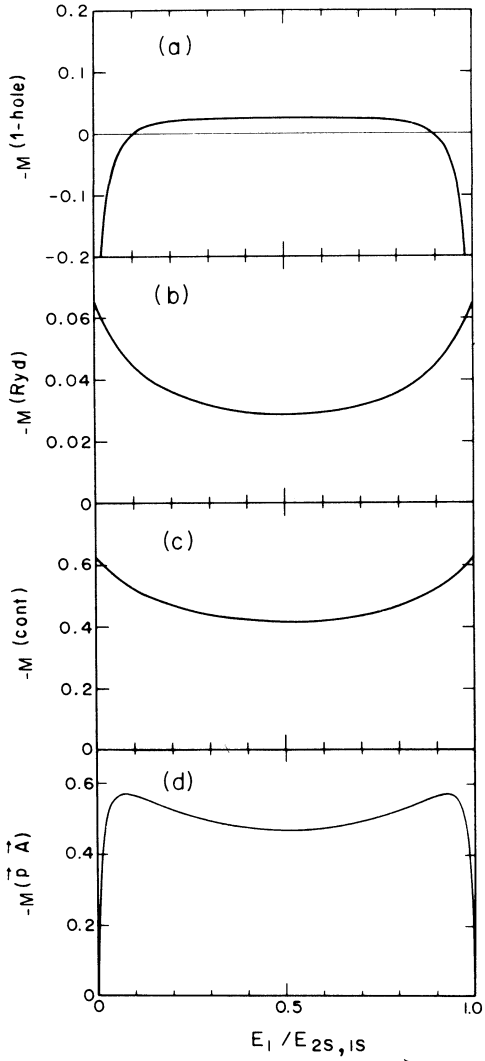

FIG. 5. Calculated contributions to $M(\vec{p}\cdot\vec{A})$ [Eq. (8c)] for the $2s \rightarrow 1s$ transition of Mo due to (a) single-hole, (b) Rydberg, and (c) continuum intermediate states. (d) $M(\vec{p}\cdot\vec{A})$, i.e., the sum of (a)–(c). This curve is compared with the experimental data in Fig. 4(a).

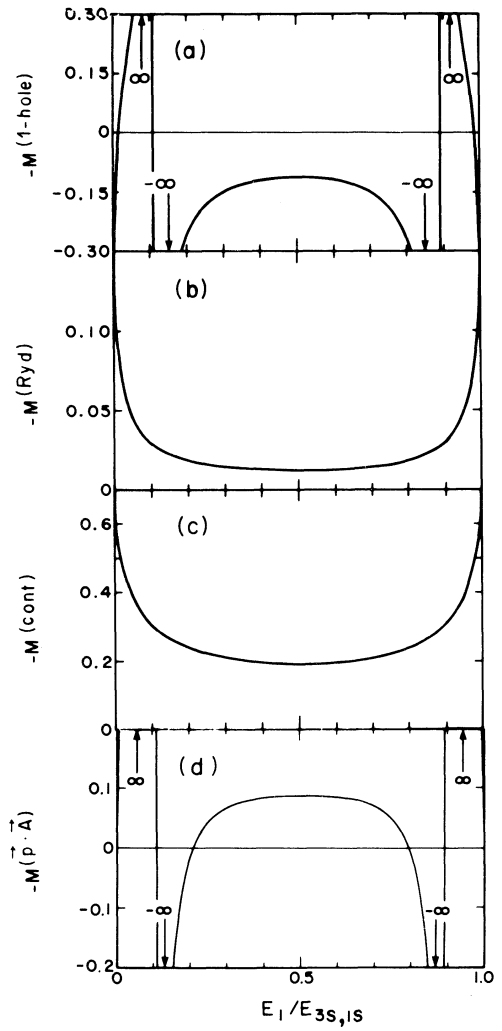

FIG. 6. Calculated contributions to $M(\vec{p}\cdot\vec{A})$ [Eq. (8c)] for the $3s\rightarrow 1s$ transition of Mo due to (a) single-hole, (b) Rydberg, and (c) continuum intermediate states. (d) $M(\vec{p}\cdot\vec{A})$, i.e., the sum of (a)—(c). All the curves in this figure and in Fig. 5 are for an angle of emission between the two photons of 90°.

Roetti.[11] The contributions of these terms are shown in Figs. 5(a) and 6(a), respectively, for the $2s\rightarrow 1s$ and $3s\rightarrow 1s$ transitions. The divergences in the results for $3s\rightarrow 1s$ are due to the intermediate $2p$ resonance.

$M^{(\mathrm{cont})}$: Following Freund[12] we make use of the fact that the absolute values squared of the matrix elements we require here appear in the expression for the appropriate photoionization cross sections σ. Accordingly, we write these matrix elements in terms of $\pm\sqrt{\sigma}$ leaving an ambiguity of sign to be resolved later. Note that this procedure is inapplicable to $md\rightarrow 1s$ since these two-photon transitions proceed via channels ($md\rightarrow p$-wave$\rightarrow 1s$), while for d states the photoionization σ involves both ($md\rightarrow p$-wave) and ($md\rightarrow f$-wave) which, in practice, are inseparable. For the required σ we use suitable empirical formulas,[14] extracting the contribution of a given shell by subtracting the contributions of all outer shells.

The empirical σ are not necessarily consistent with the wave functions of Clementi and Roetti[11] since the two yield, in general, somewhat different total oscillator strengths for the various shells.[15] Accordingly, in an attempt to improve the self-consistency of our calculations we rescale the empirical σ to make them consistent with the wave functions. In a similar vein we extract σ for the $3s$ level, for example, from that for the total M shell, by using the appropriate ratio of calculated oscillator strengths. The results for $M^{(\mathrm{cont})}$ for $2s\rightarrow 1s$ and $3s\rightarrow 1s$ are shown, respectively, in Figs. 5(c) and 6(c).

$M^{(\mathrm{Ryd})}$: For the Rydberg contribution we make use of the fact that the transition frequencies in Eq. (8c) are essentially constant and may be set equal to those of the corresponding absorption edge.[12] We may then factor out all frequency-dependent terms and so need only evaluate a sum over matrix elements. Again following Freund,[12] we evaluate this using the sum rule

$$\sum_n(\Omega_{n,I}+\Omega_{n,F})\langle I\,|\,z\,|\,n\rangle\langle n\,|\,z\,|\,F\rangle=0\ . \tag{9}$$

Here too, single-hole and (sign-ambiguous) continuum intermediate states appear and these are evaluated as described above.

We resolve the sign ambiguity of the continuum matrix elements using the (closure) sum rule

$$\langle ms\,|\,z^2\,|\,1s\rangle=\sum_n\langle ms\,|\,z\,|\,n\rangle\langle n\,|\,z\,|\,1s\rangle \tag{10}$$

and evaluating the left-hand side (lhs) directly from the wave functions of Clementi and Roetti[11] and the right-hand side (rhs) by summing the contributions of the three classes of intermediate states using the methods already described. For the lhs we obtain $\langle 2s\,|\,z^2\,|\,1s\rangle = -0.565\times 10^{-3}a_0^2$. If we choose a net positive sign for the product of continuum matrix elements we obtain for the rhs $-0.502\times 10^{-3}a_0^2$, while use of a negative sign yields $-0.11\times 10^{-3}a_0^2$. Clearly the positive sign is the proper choice here. This also proves to be the case for the $3s\rightarrow 1s$ transition. In Figs. 5(b) and 6(b), respectively, we plot the Rydberg contributions for $2s\rightarrow 1s$ and for $3s\rightarrow 1s$. Adding all contributions we plot in Figs. 5(d) and 6(d) $M(\vec{p}\cdot\vec{A})$ for $2s\rightarrow 1s$ and $3s\rightarrow 1s$, respectively.

Since our final answer is constructed from a number of seemingly disparate elements, we now inquire as to the extent to which these are mutually self-consistent. We attempt to answer this by checking additional sum rules such as

$$\langle 1s\,|\,z^2\,|\,1s\rangle=\sum_n\langle 1s\,|\,z\,|\,n\rangle\langle n\,|\,z\,|\,1s\rangle\ . \tag{11}$$

Here there are no longer any free parameters and the lhs gives $0.588\times 10^{-3}a_0^2$ while the rhs yields $0.574\times 10^{-3}a_0^2$. In general, tests such as this lead us to conclude that for the $2s\rightarrow 1s$ transition our final results should be good to about $\pm 10\%$, while for $3s\rightarrow 1s$ the errors may be as large as $\pm 30\%$. We believe that a principal reason for this relatively high degree of accuracy is the fact that the exact sum rule in Eq. (9) is built in as an intrinsic part of our answer.[12] As a result of this the Rydberg term [Figs. 5(b) and 6(b)] should probably also be viewed as a correction term that tends to compensate for the deficiencies of the other contributions. The use of Eq. (9) is also instrumen-

tal in guaranteeing that $M(\vec{p}\cdot\vec{A})$ goes to zero at the ends of the spectrum, as it is supposed to.[12] Finally, we mention that Eq. (9) is an essential step in reconciling $\vec{p}\cdot\vec{A}$ and $\vec{r}\cdot\vec{E}$ perturbation theory, so that for whatever this may be worth, our final answers are also "gauge invariant."

Since we expect that to the accuracy required here $M(\omega_1,\omega_2)=M(\vec{p}\cdot\vec{A})$, we display in Fig. 4(a) our results for $M(\vec{p}\cdot\vec{A})$ for $2s\rightarrow 1s$ superimposed upon the experimental data. Note that there are no adjustable parameters here, so that the excellent agreement implies that this transition is well understood. $M(\vec{p}\cdot\vec{A})$ for $3s\rightarrow 1s$, on the other hand, is much too small to explain the 19.7-keV two-photon transition. Accordingly, we now turn our attention to the $3d\rightarrow 1s$ transition.

We attempt an approximation suitable for the spectral midpoint $\omega_1=\omega_2=\omega$. Since ω is about half the smallest transition frequency in Eq. (8c) and is relatively less for all other terms, we make the approximation[12] $\Omega_{n,1s}-\omega\simeq\Omega_{n,1s}$. Invoking closure we immediately obtain

$$M(\vec{p}\cdot\vec{A})\simeq-\langle I\,|\,(\hat{u}_1\cdot\vec{\nabla})(\hat{u}_2\cdot\vec{r})+(\hat{u}_2\cdot\vec{\nabla})(\hat{u}_1\cdot\vec{r})\,|\,F\rangle\ . \tag{12}$$

This result, of course, implies a flat spectrum, in full accord with the data of Fig. 4. Summing over the four independent combinations of photon polarizations we obtain for $ms\rightarrow 1s$ transitions,

$$|M(\vec{p}\cdot\vec{A})|^2_{ms\rightarrow 1s}=\tfrac{4}{9}(1+\cos^2\theta)\left|\left\langle R_{m0}\left|r\frac{\partial}{\partial r}\right|R_{10}\right\rangle\right|^2, \tag{13a}$$

while for the sum of the five $md\rightarrow 1s$ transitions we have,

$$|M(\vec{p}\cdot\vec{A})|^2_{md\rightarrow 1s}=\tfrac{4}{45}(13+\cos^2\theta)\left|\left\langle R_{m2}\left|r\frac{\partial}{\partial r}\right|R_{10}\right\rangle\right|^2, \tag{13b}$$

where the R_{nl} are the appropriate normalized radial parts of the wave functions and θ is the angle between the directions of photon emission. Evaluating Eqs. (13) for $\theta=\pi/2$, as is appropriate to our experiment, and computing the matrix elements using the wave functions of Clementi and Roetti,[11] we obtain the results shown in Table I. (In Table II we list the values of all matrix elements used in this work.) It may noted that Eq. (12), when compared to our "exact" results for the $2s$ and $3s$ transitions, is good to about $\pm 40\%$. For the $3d$ transitions it predicts a value of $M(\omega_1,\omega_2)$ which is a factor of 3 smaller than the experimental value for the 19.7-keV transition, still leaving open, therefore, the question as to the origin of this transition.

Recently Florescu[16] has obtained elegant, closed-form analytical expressions for the $3s$ and $3d$ two-photon transitions of hydrogen. Her results are also shown in Table I and indicate that for this system the total effective amplitude of the $3d$ transiitions is about twice that for the $2s$ transition. We believe that this provides a sufficient *prima facie* case for the tentative identification of our 19.7-keV peak as being due primarily to the $3d\rightarrow 1s$ two-photon transition.

CONCLUSIONS AND SUMMARY

Some of the more interesting questions raised by these initial results are the following. (i) Are the spectra of Fig. 4 truly smooth, or is there important structure hidden in the noise? (ii) What would Fig. 3(a) look like under substantially higher resolution? (iii) Because of its dependence on intermediate states which sample the whole excitation spectrum of the system, is two-photon x-ray emission more sensitive to chemical and structural effects than is the case for one-photon emission? (iv) How important are two-electron processes, the backscattering of the (here virtual) outgoing wave which gives rise to extended x-ray absorption fine structure, and the many-body effects which give rise to absorption-edge singularities? (v) Do the main features of the two-photon emission vary smoothly across the Periodic Table, or does the interplay between the various competing contributions shown in Figs. 5 and 6 lead to large Z-dependent variations?

These and many other questions can be answered from the theoretical point of view by using techniques that go substantially beyond the simple, one-electron picture em-

TABLE I. Absolute values of the matrix elements governing two-photon emission for various transitions. Listed are the values at the spectral midpoint for an angle of 90° between the directions of photon emission. The entries for d states are the root-square sum over the five different d states. The entries for Mo are based on the wave functions of Clementi and Roetti (Ref. 11). Also listed are results for a hydrogenic model with $Z=42$. Note that the $\vec{p}\cdot\vec{A}$ matrix elements are independent of Z.

m	$\vec{p}\cdot\vec{A}$ $ms\rightarrow 1s$ Mo [Eq. 8(c)]	$\vec{p}\cdot\vec{A}$ $ms\rightarrow 1s$ Mo [Eq. 13(a)]	$\vec{p}\cdot\vec{A}$ $ms\rightarrow 1s$ H atom [Eq. 8(c)]	$\vec{p}\cdot\vec{A}$ $md\rightarrow 1s$ Mo [Eq. 13(b)]	$\vec{p}\cdot\vec{A}$ $md\rightarrow 1s$ H atom [Eq. 8(c)]	A^2 $mp\rightarrow 1s$ Mo [Eq. 8(b)]	A^2 $mp\rightarrow 1s$ H atom [Eq. 8(b)]	Expt. (Fig. 4)
2	0.47	0.34	0.55[a]			0.11	0.11	0.45
3	0.09	0.12	0.21[b,c]	0.20	1.05[c]	0.04	0.05	0.54
4		0.05		0.05				
5		0.01						

[a]F. Bassani, J. J. Forney, and A. Quattropani, Phys. Rev. Lett. 39, 1070 (1977).
[b]A. Quattropani, F. Bassani, and S. Carillo, Phys. Rev. A 25, 3079 (1982).
[c]V. Florescu (private communication).

TABLE II. Matrix elements for Mo (in units of a_0 or a_0^2) used in evaluating Eqs. (8) and (13) and the various sum rules used in this work. The wave functions are from Clementi and Roetti (Ref. 11).

$\langle 1s \mid z \mid 2p \rangle$	-1.672×10^{-3}	$\langle 2s \mid z \mid 2p \rangle$	8.176×10^{-2}
$\langle 1s \mid z \mid 3p \rangle$	5.473×10^{-3}	$\langle 2s \mid z \mid 3p \rangle$	3.654×10^{-2}
$\langle 1s \mid z \mid 4p \rangle$	1.923×10^{-3}	$\langle 2s \mid z \mid 4p \rangle$	1.089×10^{-2}
$\langle 2p \mid z \mid 3s \rangle$	-1.774×10^{-2}	$\langle 2p \mid z \mid 3d \rangle$	-8.407×10^{-2}
$\langle 2p \mid z \mid 4s \rangle$	5.175×10^{-3}	$\langle 2p \mid z \mid 4d \rangle$	1.747×10^{-2}
$\langle 3p \mid z \mid 3s \rangle$	-2.502×10^{-1}	$\langle 4p \mid z \mid 3s \rangle$	5.178×10^{-2}
$\langle 1s \mid z^2 \mid 1s \rangle$	5.878×10^{-4}	$\langle 2s \mid r\partial/\partial r \mid 1s \rangle$	5.151×10^{-1}[a]
$\langle 2s \mid z^2 \mid 2s \rangle$	9.833×10^{-3}	$\langle 3s \mid r\partial/\partial r \mid 1s \rangle$	1.849×10^{-1}[a]
$\langle 1s \mid z^2 \mid 2s \rangle$	-5.652×10^{-4}	$\langle 4s \mid r\partial/\partial r \mid 1s \rangle$	-7.042×10^{-2}[a]
$\langle 3s \mid z^2 \mid 1s \rangle$	-1.790×10^{-4}	$\langle 5s \mid r\partial/\partial r \mid 1s \rangle$	1.792×10^{-2}[a]
$\langle 3s \mid z^2 \mid 3s \rangle$	7.298×10^{-2}	$\langle 3d \mid r\partial/\partial r \mid 1s \rangle$	1.843×10^{-1}[a]
		$\langle 4d \mid r\partial/\partial r \mid 1s \rangle$	4.735×10^{-2}[a]

[a]Radial part.

ployed here. Experimentally, very significant improvements in signal-to-noise ratios and modest improvements in resolution can be anticipated using currently available technology. As regards resolution, a net factor of 3 should be possible due to recent advances in the fabrication of large-area semiconductor detectors and the use of a window much less than 1 keV in the construction of graphs such as those in Figs. 3 and 4. A narrow window, of course, will require greatly improved signal levels. One may expect to extend the limiting $\sim10^4$/sec count-rate per detector by a factor of 3 or more, while another large factor is available at the cost of a modest increase in the number of detectors employed. It may easily be seen that the total number of coincidences recorded by N detectors each of which collects a solid angle $\Delta\Omega$ is proportional to $N(N-1)(\Delta\Omega)^2$, so that doubling the number of detectors from two to four leads to a sixfold improvement in count rate. Since most of the logic is handled anyway by the microcomputer, the additional complexity of the required circuitry is not extensive. Accordingly, we anticipate that with these and other improvements both in technique and in theory, two-photon inner-shell spectroscopy will prove to be a rich new source of information on atomic and related processes.

ACKNOWLEDGMENT

We are pleased to acknowledge many important contributions by Professor Joel I. Gersten.

APPENDIX

We consider briefly here a number of interfering processes that conceivably could make measurable contributions to our apparent two-photon spectra.

Atomic cascades. In Mo itself, for example, the initial K-shell vacancy will generally lead to a cascade in which the vacancy is filled by an L-shell electron emitting a K-line photon, followed by an M-shell electron filling the resulting L-shell vacancy with emission of an L-line photon. Since both the K lines (in the region 17—20 keV) and the L lines (in the region 2—3 keV) are outside our 4—14-keV window, this particular atomic cascade does not contribute to our spectra. However, impurity elements much lighter or heavier than Mo can produce photons within the 4—14-keV window.

Light elements (such as Zn) can produce pairs of K-line photons (8.6 keV) due to double K-shell vacancy production in a single atom induced by absorption of the Ag $K\alpha$ radiation.[17] Indeed, we easily observed such processes during our *in situ* energy calibration procedure. In our experiment, however, noncredibly large impurity concentrations are required due to the fact that the efficiency of double-vacancy production is $\sim10^{-2}-10^{-3}$ single-vacancy production. Further, in spectra such as those in Fig. 4, this process yields a single sharp line at approximately the $K\alpha$ energy, rather than a smooth continuum. We note in passing that an apparatus such as ours provides a sensitive tool easily exploited for the study of this interesting two-electron, one-photon process.

In very heavy elements complex combinations of radiative and Auger cascades can, in some instances, produce photons within our 4—14-keV window and could be observed at parts per million (ppm) impurity concentrations. Such cascades, of course, would also produce sharp lines in Fig. 4, which, however, are not observed. In future work with improved resolution and signal-to-noise ratio, this problem may require more careful consideration.

Double-Compton scattering. In this two-photon analog of Compton scattering, two outgoing quanta are produced. These form a continuum with an energy sum less than that of the incident photon by something of the order of the Compton shift. (The kinematics here are slightly different than in ordinary Compton scattering because two quanta are produced instead of one.) For our geometry the Compton shift of the incident 22-keV Ag $K\alpha$ radiation is about 1 keV. Furthermore, in analogy to ordinary Compton scattering, the initial-state momentum distribution of the electrons must produce a relatively broad profile for the energy sum, so that double-Compton scattering could conceivably make a significant contribution to our 19.7-keV peak. Levine and Freund[7] give an expression appropriate to our experiment for $(d\dot{N}_{DC}/d\omega)/\dot{N}_{\mathrm{Ag}}$, their Eq. (12), where $\dot{N}_{DC}$ is the emission rate of double-Compton photons and $\dot{N}_{\mathrm{Ag}}$ is the incident Ag K flux. For purposes of comparison, the two-

photon emission count rate may be similarly written as

$$\frac{1}{\dot{N}_{\mathrm{Ag}}}\frac{d\dot{N}_2}{d\omega}=(1-e^{\mu_{\mathrm{Ag}}t})\frac{\omega_K}{W^{(1)}}\frac{dW^{(2)}}{d\omega} \tag{A1}$$

using the rate equation for K-shell vacancy production, the definition of the fluorescence efficiency ω_K, and Eq. (6b). Here μ_{Ag} is the absorption coefficient of Mo for Ag $K\alpha$ radiation, and t the effective sample thickness. Both the 100-nm Mo film and its 6-μm Mylar support contribute to the double-Compton scattering, with the intensity due to the Mylar being ~ 3 times that due to the Mo. Their combined contribution, however, is calculated to be about 10^{-3} of the two-photon intensity so that under the conditions of our experiment double-Compton scattering is not significant. This might not be the case, however, under very different conditions.

Multiple bremsstrahlung. Approximately half the initial K-shell vacancies in Mo are filled by Auger processes. These yield electrons with kinetic energies between ~ 14—17 keV. An approximately equal number of electrons with kinetic energies between ~ 19—22 keV are produced by direct photoionization. All these electrons rattle around inside the Mo film and its support, losing energy by ionization and by bremsstrahlung. The thick-target efficiency of bremsstrahlung is $\sim 10^{-9}ZV$, where eV is the electron kinetic energy and Z the target nuclear charge. For our case this efficiency is $\sim 10^{-3}$. The bremsstrahlung spectrum is a continuum which covers our 4—14-keV window, but because it consists ordinarily of single-photon events, these should cause no particular problems. Of course, a small fraction of the energy released occurs in two-step processes which yield two photons in apparent time coincidence. The efficiency of such multiple processes is of the order of the square of that for the one-step process, i.e., $\sim 10^{-6}$, and this is approximately the efficiency of the two-photon emission relative to one-photon emission (recall that the number of electrons freed is about equal to the number of Mo K-line photons emitted). These arguments, therefore, suggest that multiple bremsstrahlung is a potentially serious source of background not easily distinguished from the two-photon emission, at least for the case of thick targets. For our thin, planar geometry, however, more detailed calculations are required. These have been performed by Gersten [J. I. Gersten (unpublished)]. His results are too complex to reproduce here, but they demonstrate that under the conditions of our experiment, multiple bremsstrahlung is not a problem. This might not be the case, however, for other experimental configurations.

There is, of course, a true two-photon bremsstrahlung. From general considerations one would expect this to be weaker than the corresponding one-photon process by a factor of order $\alpha(eV/mc^2)\approx 3\times 10^{-4}$ for ~ 20-keV electrons. Since this leads to an intensity somewhat less than that of the two-step process, which is found not be important here, we conclude that two-photon bremsstrahlung is similarly unimportant in the present experiment.

Detector cross talk. When the mask in Fig. 1 was removed, the apparent two-photon signal rate increased by about an order of magnitude. Using an apparatus similar to the one shown schematically in Fig. 7, we could demonstrate that this large increase in signal was due to photon-mediated cross talk between the detectors induced by the Mo $K\alpha$ flux. There are a large number of mechanisms possible. In all of these a Mo $K\alpha$ photon deposits its energy in one detector via a process that subsequently produces a lower-energy photon which reaches the second detector.

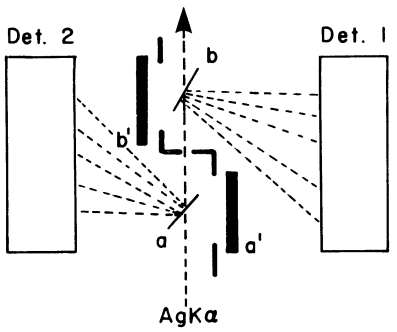

FIG. 7. Schematic of arrangement used to study detector cross talk. Samples a and b and masks a' and b' are separately removable. Direct photon-mediated cross talk was, for example, measured by removing both sample b and mask b'. The actual apparatus is three dimensional in nature, as in Fig. 1, and contains various other apertures and masks.

In the detector material itself, Si, the primary detection process involves production of an Si K-shell vacancy. If this is filled radiatively, the emitted Si K lines may escape and reach the second detector. Since these particular photon energies are only ~ 1.75 keV, neither single- nor double-vacancy production yield signals within our 4—14-keV window. However, a wide range of impurities at multi-ppm concentrations are calculated to make measurable contributions to the cross talk, as does the thin front-surface gold electrode of the Si crystal. Other relevant mechanisms involve ordinary bremsstrahlung from the primary photoelectron and the infrared divergence of the Compton effect.[18] These latter processes are expected to yield measurable intensities and an energy summation spectrum having sharp peaks at the Mo $K\alpha$ and $K\beta$ energies, thereby closely mimicking Fig. 3(a). Accordingly, such processes are potentially fatal unless their intensities are strongly reduced by proper masking.

Although calculation indicates that none of the above make a measurable contribution to our data when the mask is in place, we have not, because of the extreme dangers involved, been content to rely on this, especially since we are unable to quantitatively account for the observed magnitude of the cross talk without the mask. Using an arrangement which is in the spirit of Fig. 7 but which exploits the three-dimensional nature of our apparatus, we have performed an extensive series of meaurements testing directly the magnitude of the cross talk as a function of sample nature, placement, thickness, and de-

gree and kind of masking. These demonstrate conclusively that with the arrangement of Fig. 1, our standard arrangement, detector cross talk is negligible compared to our observed two-photon signal. It is worthwhile reiterating that in any experiment involving detection of a weak two-photon process in the presence of a much stronger one-photon flux, the problem of detector cross talk must be examined exhaustively.

[1]M. Göppert-Mayer, Ann. Phys. (Leipzig) 9, 273 (1931).

[2]R. Novick, in *Physics of One- and Two-Electron Atoms,* edited by F. Bopp and H. Kleinpoppen (North-Holland, Amsterdam, 1969), pp. 295–325; M. Lipeles, R. Novick, and N. Tolk, Phys. Rev. Lett. 15, 690 (1965); C. J. Artura, N. Tolk, and R. Novick, Astrophys. J. Lett. 157, L181 (1969); C. A. Kocher, J. E. Clendenin, and R. Novick, Phys. Rev. Lett. 29, 615 (1972); E. A. Hinds, J. E. Clendenin, and R. Novick, Phys. Rev. A 17, 670 (1978).

[3]R. Marrus and R. W. Schmieder, Phys. Rev. A 5, 1160 (1972); Phys. Lett. 32A, 431 (1970); Phys. Rev. Lett. 25, 1689 (1970); R. W. Schmieder and R. Marrus, *ibid.* 25, 1245 (1970); 25, 1692 (1970); R. Marrus, in *Atomic Physics,* edited by S. J. Smith and W. G. King (Plenum, New York, 1972), Vol. 3, pp. 291–308.

[4]M. H. Prior, Phys. Rev. Lett. 29, 611 (1972); D. O'Connell, K. I. Kollath, A. J. Duncan, and H. Kleinpoppen, J. Phys. B 8, L214 (1975); H. Kruger and A. Oed, Phys. Lett. 54A, 251 (1975); C. L. Corke, B. Cornutte, J. R. MacDonald, J. A. Bednar, and R. Marrus, Phys. Rev. A 9, 2242 (1974); C. L. Corke, B. Cornutte, and R. Randall, Phys. Rev. Lett. 31, 507 (1973); H. Gould, R. Marrus, and R. W. Schmieder, *ibid.* 31, 504 (1973). See also, P. Braunlich and P. Lambropoulos, *ibid.* 25, 135 (1970); 25, 986 (1970); P. Braunlich, R. Hall, and P. Lambropoulos, Phys. Rev. A 5, 1013 (1972); H. Gould and R. Marrus, *ibid.* 28, 2001 (1983).

[5]Y. B. Bannett and I. Freund, Phys. Rev. Lett. 49, 539 (1982); Y. B. Bannett, Ph.D. thesis, Bar-Ilan University, Ramat-Gan, Israel, 1982.

[6]Incoherent double-quantum scattering by *free* electrons was first discussed by W. Heitler and L. Nordheim, Physica (Utrecht) 1, 1059 (1934). More recent calculations include M. Ram and P. Y. Wang, Phys. Rev. Lett. 26, 476 (1971) and references contained therein. See, also M. Ram and P. Y. Wang, *ibid.* 26, 1210(E) (1981); K. J. Mork, Phys. Rev. A 4, 917 (1971); review by J. H. Hubbell, W. J. Veigele, E. A. Briggs, R. T. Brown, D. T. Cromer, and R. J. Howerton, J. Phys. Chem. Ref. Data 4, 471 (1975).

[7]Both coherent and incoherent double-quantum scattering by *bound* electrons (appropriate to the present experiment) are discussed by B. F. Levine and I. Freund, Opt. Commun. 3, 197 (1971).

[8]H. A. Bethe and E. R. Salpeter, *Quantum Mechanics of One- and Two-Electron Atoms* (Springer, Berlin, 1957), Sec. 67; S. P. Goldman and G. W. F. Drake, Phys. Rev. A 24, 183 (1981). For Mo ($Z=42$) relativistic effects change $W^{(2)}$ by only 6%.

[9]J. J. Sakurai, *Advanced Quantum Mechanics* (Addison-Wesley, Reading, Mass., 1967).

[10]The detectors were constructed to our specifications by Seforad Ltd., Emek Hayarden, Israel.

[11]E. Clementi and C. Roetti, At. Data Nucl. Data Tables 14, 177 (1974).

[12]I. Freund, Phys. Rev. A 6, 1849 (1973).

[13]T. Aberg, in *Atomic Inner-Shell Processes,* edited by B. Crasemann (Academic, New York, 1975), Vol. I, pp. 353–359.

[14]W. H. McMaster, N. K. Del Grande, I. H. Mallett, and J. H. Hubbell, Lawrence Livermore Radiation Laboratory Report No. UCRL-50174, Sec. II, Rev. 1 (1969) (unpublished).

[15]R. W. James, *The Optical Principles of the Diffraction of X-rays* (Cornell University Press, Ithaca, N. Y. 1965) Chap. IV.

[16]V. Florescu (private communication).

[17]S. I. Salem, A. Kumar, K. G. Schiessel, and P. L. Lee, Phys. Rev. A 26, 3334 (1982) and references cited therein.

[18]Y. B. Bannett, J. I. Gersten, N. Tzoar, and I. Freund, Phys. Rev. Lett. 36, 882 (1976).